Acoust. Sci. & Tech. **43**, 5 (2022)

PAPER

Integrity assessment of turbine generator rotor wedges based on their resonance characteristics

Yuji Wada[1,*], Kentaro Nakamura[1], Kota Sadamoto[2], Hiroshi Araki[2] and Wataru Tsujita[2]

[1]*FIRST, Tokyo Institute of Technology, Yokohama, 226–8503 Japan*
[2]*Advanced Technology R&D Center, Mitsubishi Electric Corporation, Amagasaki, 661–8661 Japan*

(*Received 11 March 2022, Accepted for publication 3 June 2022*)

Abstract: The integrity evaluation of the rotor wedges of turbine generators is discussed by observing the mechanical resonant frequency shift originating from cracks. We propose a simple method of obtaining the frequency response of the inspection target using point contact piezoelectric sensors and a network analyzer. Eigenmodes are identified in both experiments and finite element analysis, and frequency responses are compared. Several resonant frequencies shift to the lower side owing to the stiffness decrease caused by the crack, and the validity and effectiveness of the method are discussed. From both measurements and finite element analysis (FEA), the modes where the crack is located in the high-stress region have a more significant shift than the mode that does not. The shift was correlated between the FEA and measurement throughout most of the modes.

Keywords: Nondestructive testing, Turbine generator rotor wedge, Resonant frequency shift, Finite element analysis

1. INTRODUCTION

The rotor wedges of a turbine generator [1–4] hold a large centrifugal force acting on the rotor coil in the slots of the rotor iron core. After a prolonged operation, cracks may appear on the part of a wedge that hooks into the slot, as shown in Fig. 1. A conventional industrial method enables the detection of cracks of 0.5 mm or deeper [5]. To prevent a catastrophic breakdown, periodic health diagnoses should be performed. Cracks themselves can be detected visually if every wedge is removed from the slots. However, it is a labor-intensive task to perform such an inspection for hundreds of wedges.

The MHz-band ultrasonic pulse-echo method [6] is commonly used to nondestructively detect cracks of less than 1 mm depth. However, the method has several disadvantages, such as it requires a long measurement time because the entire surface of the part being studied must be scanned. Furthermore, it cannot detect defects located in the shadow region of the ultrasonic beam owing to the uneven shape of the wedge. In addition, the inspection surface, which is usually covered with dust, should be cleaned.

*e-mail: ywada@sonic.pi.titech.ac.jp
[doi:10.1250/ast.43.260]

Many other methods have been proposed for nondestructive testing using ultrasound. Linear methods focus on vibration intensity [7], strain energy [8], or guided waves [9–13]. Electromagnetic acoustic transducers (EMATs) [9,14,15] are sometimes used for driving and detecting ultrasonic vibration. Nonlinear methods such as imaging using harmonics of airborne ultrasound [16,17] and nonlinear scattering from closed cracks [18–20] have also been proposed. In recent years, resistance detection by ultrasonic heating [21] and defect detection by guided wave generation using an airborne ultrasonic phased array [22] have been reported.

If the focus of the inspection is not on the crack location but on the integrity of the component, inputting a broadband signal and detecting changes in the frequency spectrum of the component, which is measured in a healthy state beforehand, can be an effective method [23,24]. Ghosh *et al.* [10] and Kundu [12] inputted a wideband signal to a specimen plate submerged in water and detected defects from the fluctuations of multiple Lamb wave modes. Koyama *et al.* [25] investigated a method of estimating the amount of liquid in a sealed cylindrical tank from the resonant frequency shift of an inserted metal rod because of the mass-loading effect of liquid. Hasebe *et al.* [26] evaluated the soundness of the amount of adhesive material from the resonant frequency shift of anchor bolts

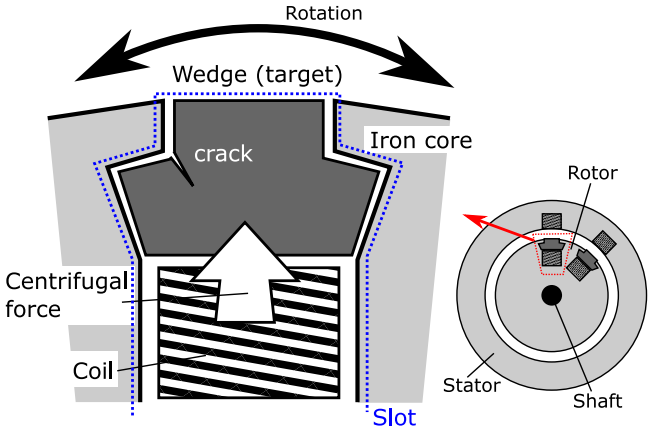

Fig. 1 Cross section of rotor wedge and common location of crack.

driven by EMATs. Takata *et al.* [27] diagnosed the aging of piping from the resonant frequency shift of the in-plane bending deformation vibration of cylindrical shells attributed to the stiffness change.

For ultrasonic crack detection and evaluation, numerical analysis is used in combination with the above methods, especially for the visualization of scattering. Finite difference analysis [28,29] is suitable for handling time waveforms with low memory usage. Finite element analysis (FEA) [30,31] has the advantage of modeling complex geometries and using both eigenvalue and frequency domain analysis. Boundary element analysis [32] and the distributed point source method [12,33] are effective for analysis with few interfaces because they can handle open regions.

We have studied a method using a point-contact piezoelectric sensor to measure the frequency responses of a specimen to detect the existence of cracks. The advantages of the method are as follows.

(1) Detection is possible using inexpensive sensors and a low-cost USB-based network analyzer.
(2) Measurement is completed in a few minutes by pressing the sensor against two fixed points on the sample.
(3) Inspection is possible for an entire component, including the shadow zone of a MHz-ultrasonic beam.
(4) The sensor head has a small round shape and easily penetrates oil or dust on the surface.
(5) Inspection is possible without removing wedges from rotor slots.

In this paper, we describe the proposed inspection method and the structure of the piezoelectric sensor, and investigate the crack detection capability for a metallic member using the resonant frequency shift. First, as a preliminary test of the proposed inspection concept, we conduct crack detection in a two-dimensional T-shaped component. Second, we apply the method to an actual wedge component for practical application. Furthermore, we discuss the relationship between crack-susceptible modes and the stress distribution through FEA.

The FEA simulation was performed to grasp the resonance frequencies and their corresponding mode shapes, as well as the effects of cracks on the frequency shifts. However, we do not pursue an exact match between the measured frequencies and the calculated results. This is because the actual wedges made with the same design exhibited a slight individual difference in the resonance frequencies, which might be caused by a production process. This also means that cracks cannot be detected from only the post-operational frequency response, but the initial frequency response must be obtained in a healthy state beforehand.

2. PRELIMINARY TEST USING TWO-DIMENSIONAL T-SHAPED METAL BLOCK

2.1. Target Specimen and Analysis Model

Figure 2(a) depicts the T-shaped test piece made of structural steel (SS400). Specimens with different sizes of crack are prepared. The crack depth is $d = 0$–3 mm (every 0.5 mm), the width is $w = 1$ mm, and the vertical position is $y = 1$ mm from the T-junction to mimic the crack-prone area indicated in Fig. 1. Owing to the restriction of the machining available at the laboratory, the crack width was $w = 1$ mm, which was larger than a practical one.

Figure 2(b) illustrates the configuration of the point-contact sensor. The sensor consists of a multilayered piezoelectric actuator (PC4FL, Thorlabs Inc.), a convex lens of $R = 4.2$ mm, and a 13-mm-long back mass. The multilayered actuator is employed to be driven with a few volts of the output voltage by the network analyzer used in Sect. 3. The convex lens increases the setting precision of the sensor relative to the surface. Since the lens and the target surface are in point contact, changes in the vibration

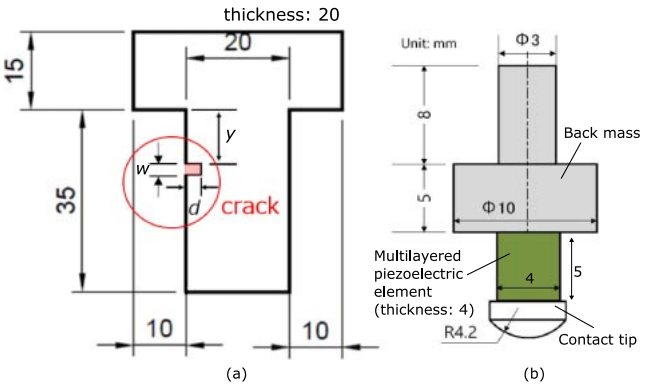

Fig. 2 (a) T-shaped specimen for preliminary test and (b) point-contact sensor.

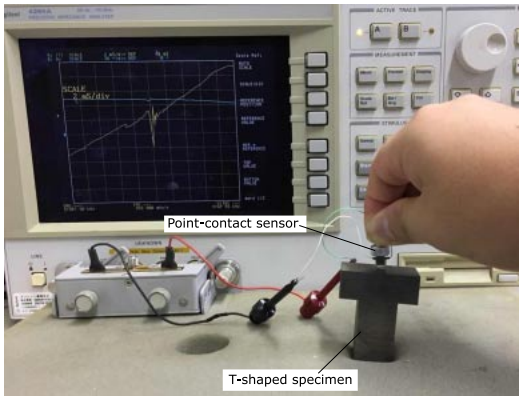

Fig. 3 Photograph of measurement setup.

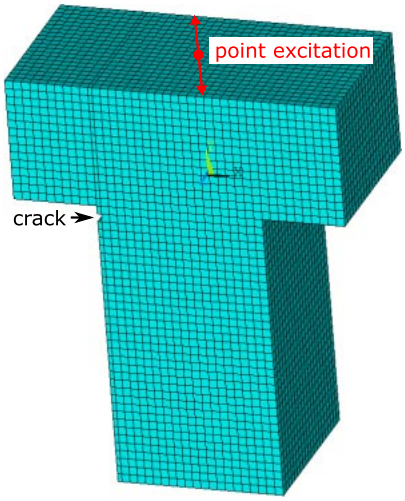

Fig. 4 Finite element model of T-shaped specimen.

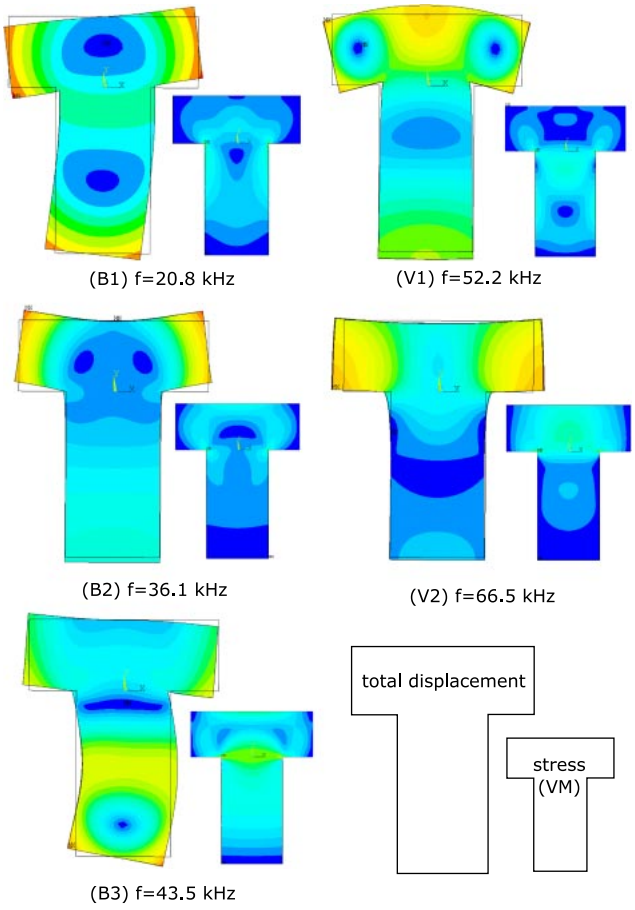

Fig. 5 Bending and longitudinal vibration modes in the range of 20–100 kHz. Contours show the amplitude of displacement and von Mises stress.

characteristics of the test object caused by the sensor. The round shape of the lens provides freedom for the direction precision in placing the sensor on the specimen surface. In the preliminary test, we used a single sensor and obtained the frequency spectrum of the electrical admittance using an impedance analyzer (4294A, Agilent). Figure 3 is a photograph of the measurement setup. Measurement was performed by pressing the convex lens of the sensor with a hand against the center of the top surface of the T-shaped test piece on the sponge sheet.

Figure 4 shows the finite element model, which is divided into 1 mm elements and has typical material parameters of steel: Young's modulus of 210 GPa, Poisson's ratio of 0.3, and density of 7,800 kg/m^3. The analysis was performed using commercial FEA software (ANSYS 2019 R3) with three-dimensional quadratic 20-node hexahedral elements (SOLID186). A node on the middle of the upper surface of the T-shape is excited by external vertical force input. Figure 5 shows the displacement amplitudes and stress distributions for the eigenmodes existing in the frequency range of 20–80 kHz in a healthy member. Modes with asymmetric distributions in the depth direction, such as torsion in the longitudinal bars, which hardly occurs in an actual wedge with the current excitation method, are excluded. In all of the above modes, the stress is high near the T-junction. If a crack occurs in this area, the resonant frequency is expected to decrease owing to a reduction in stiffness.

2.2. Frequency Response

Figure 6(a) shows the frequency response of the vibration displacement for 20–80 kHz (every 100 Hz) with a unit load input simulated with the finite element method. Since the driving point is located at the center of the structure, only the (V1) and (V2) longitudinal vibration modes can easily be observed. Figure 6(b) shows the measured electrical admittance characteristics in the same frequency settings. The prominent peak and dip originating from the electrical characteristics of the piezoelectric element should be excluded from our interest, but the small change around 52 kHz is more noteworthy, and this is the response of the (V1) mode. The upward global slope in the measured curves was due to the electrical capacitance

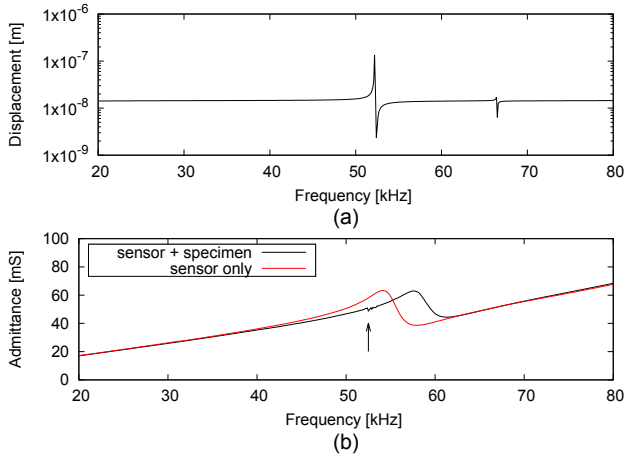

Fig. 6 Frequency responses of (a) displacement with FEA and (b) measured admittance.

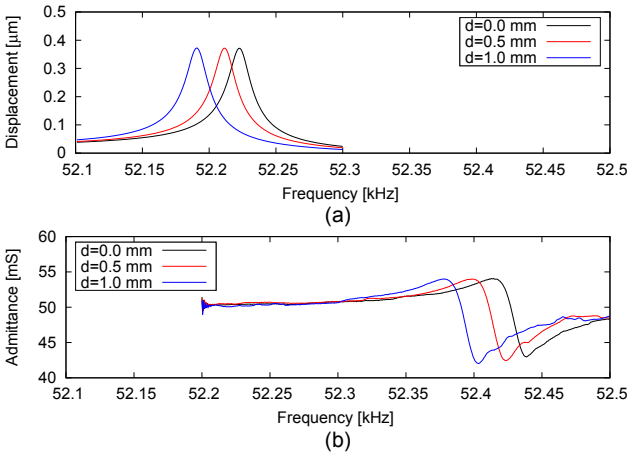

Fig. 7 Frequency responses near (V1) mode of (a) displacement with FEA and (b) measured admittance.

of the multilayered piezoelectric actuator. We can hardly observe the (V2) mode in the electrical measurement. Therefore, in the following, we focus on the data in the vicinity of the (V1) mode.

Figure 7 shows the frequency response near the (V1) mode for different crack depths in every 0.5 Hz. Figure 7(a) shows the displacements calculated with the finite element method, while Fig. 7(b) shows the measured admittances. Although the third significant digit of the frequency differs between the calculated and measured data owing to the drift in the measurement temperature and the possible error in workpiece dimensions, the peak shifts ($\Delta f = f_{\text{crack}} - f_{\text{no-crack}}$) for the same crack depth are almost identical: -13 Hz (error: 3 Hz) for a depth of 0.5 mm and -35 Hz (error: 5 Hz) for a depth of 1.0 mm, where the error is defined to be $|\Delta f_{\text{measure}} - \Delta f_{\text{FEA}}|$.

Figure 8 shows the dependence of the peak shift rate ($\Delta f / f_{\text{no-crack}}$) on the crack depth. The FEA results also show the shifts for eigenmodes other than the (V1) mode.

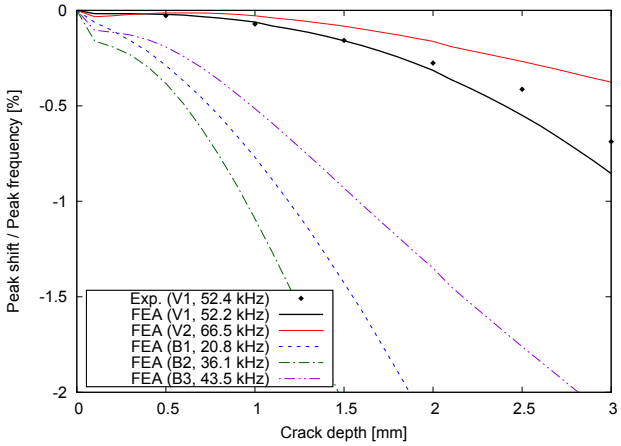

Fig. 8 Peak shift rate dependence on crack depth.

Although the original peak positions are not exactly the same, the experimental and analytical peak shifts agree within an average error of 20%. The relatively abrupt change in the vicinity of depth = 0.1 mm in the FEA results can be attributed to a numerical factor; that is, the element stiffness tends to be higher than in reality because the FEA element near the crack becomes thin and hexahedral with a high aspect ratio [34]. The peak shift is more than ten times larger for the (B1) mode than the (V1) mode. Therefore, if we wish to actively use the (B1) mode to obtain larger shifts, we should change the excitation position to the left or right edge of the upper side of the T-shape. However, it is impossible to access the corresponding part in an actual generator wedge, the left or right end of the bottom surface in Fig. 1, since the iron core slot entirely covers it.

2.3. Discussion

In this section, the effectiveness of the above crack detection method is discussed. Steel parts of industrial machinery are usually designed with a safety factor of about $k_s = 2$ [3]. The yield stress [35] of mild steel (SS400) is $\sigma_y = 240$ MPa, and the fracture toughness [36,37] is generally considered to be $K_I = 200\,\text{MN/mm}^{3/2}$. The critical crack depth d_c at which crack propagation proceeds at the design stress for a one-sided crack in a uniform bar is derived from [38]

$$K_I = \frac{\sigma_y}{k_s}\sqrt{\pi d_c}, \tag{1}$$

giving $d_c = 0.9$ mm. To avoid structure breakdown, we should detect a crack of this depth ($d_c = 0.9$ mm) or greater. In the above experiment, we can detect the crack with the target depth of 0.5 mm from the peak shift of 10 Hz with good signal-to-noise ratio. The crack is considered to be sufficiently detectable as long as the sampling frequency is 10 Hz or lower.

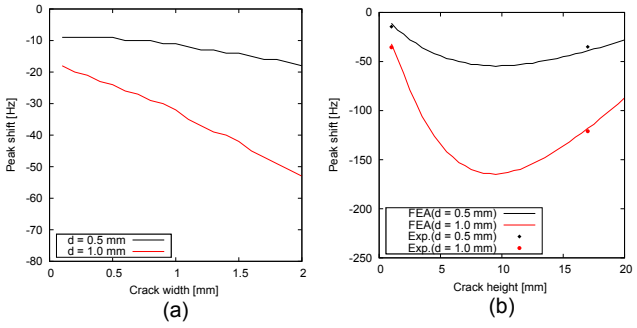

Fig. 9 Peak shift dependence on crack (a) width w and (b) height y.

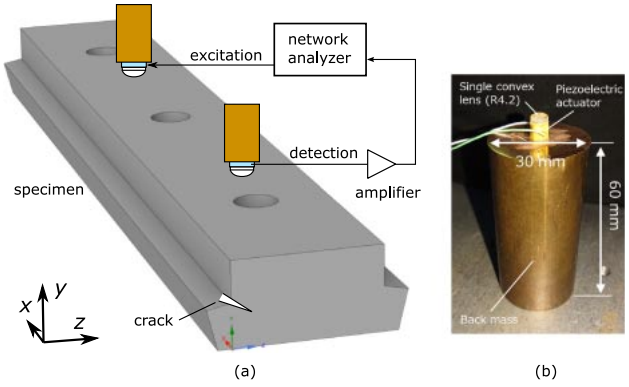

Fig. 10 (a) Wedge specimen, common location of crack, and measurement setup and (b) point-contact sensor.

The possibility of false negatives should be discussed numerically when the crack width w is less than 1 mm, or the crack is located farther away from the T-junction. Figure 9 shows the change in frequency shift when the crack (a) width w and (b) crack height y are changed for the crack depths $d = 0.5$ and 1.0 mm. The experimental results for $y = 17$ mm are also plotted in (b) because we have already measured such a sample case. Since the frequency shift is caused by the decrease in elasticity in the high-stress region shown in Fig. 5, the effect of the crack width w is not so significant that a frequency shift of about 10 Hz is observed even when the crack width is almost zero. Regarding the crack height y, the frequency shift tends to increase as it moves away from the T-junction up to 10 mm. There is a possibility that the shift approaches zero above a height of 20 mm, but this is not a problem because this height is sufficiently far from the crack-prone area.

Since the peak shift depends on the crack depth, width, and position, it is impossible to identify the crack depth and position from the frequency shift of a single mode. However, if the frequency response of the healthy state is obtained beforehand, it can be used to determine whether a part is in a healthy or unhealthy state.

3. TEST WITH THREE-DIMENSIONAL WEDGE

3.1. Measurement Settings and Resonant Modes

In this section, we apply the proposed method to a practical three-dimensional wedge. Figure 10(a) illustrates the test piece to be inspected [39], the crack-prone area, and the measurement method. The target part is made of stainless steel with a length of 300 mm, a width of 51 mm, and a height of 25 mm, and has three through holes. Hundreds of wedges are installed in a practical large turbine generator, and the accessible surface for inspection is the top one shown in the figure.

A set of multilayered piezoelectric elements with brass back masses and convex lenses bonded to them is used as an exciter and sensor. A chirp signal is input to one of the piezoelectric elements located at a quarter length from one end to excite vibration. The other element receives the vibration at a quarter length from the other end to obtain its transfer function. The transfer function is measured to avoid the electrical capacitance effect observed in Fig. 6. In the sensor shown in Fig. 10(b), the back mass in Fig. 2(b) is replaced with a brass cylinder having a higher mass to keep the pressing condition constant using gravity. The test wedge is placed on the sponge sheet, and the two elements are held by hand during the measurement. A low-noise preamplifier (ITHACO, 1201 Low Noise Pre-amplifier) is employed to increase the output signal by a factor of 20. The expensive network analyzer was replaced by Analog Discovery 2 (Digilent Inc.), a low-cost USB-based analog circuit measurement tool, to acquire the transfer function. The low-cost measurement tool worked well for our purpose because it exhibited enough frequency accuracy and stability owing to the quartz-oscillator-based clock. Although the absolute precision in the magnitude of transfer function was poorer than the impedance analyzer, the absolute magnitude was not necessary for the proposed method. Owing to the electrical capacitance of the sensor head, the input voltage of 5 V drops by half between 20 and 40 kHz. Therefore, the evaluation is based on the gain of the transfer function between the input and output voltages, $G_V = |V_{\text{out}}/V_{\text{in}}|$.

Figure 11 is a photograph of a crack formed to mimic a typical one. A wire cutter was used to make a 0.3-mm-wide, 5-mm-deep incision at the preferred location of the crack at an angle of elevation of 45° and an angle of azimuth of 60°. A 10-mm-long cut is visible in front of the crack. After measuring the frequency response of the sound member, the artificial crack was created, and the frequency response was measured again.

Figure 12 depicts the finite element model with a crack (i). The wedge part with a crack is divided into

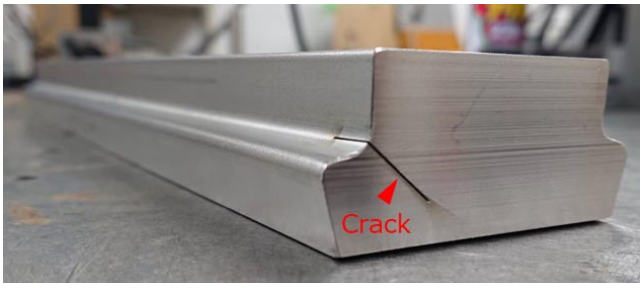

Fig. 11 Photograph of specimen with simulated crack.

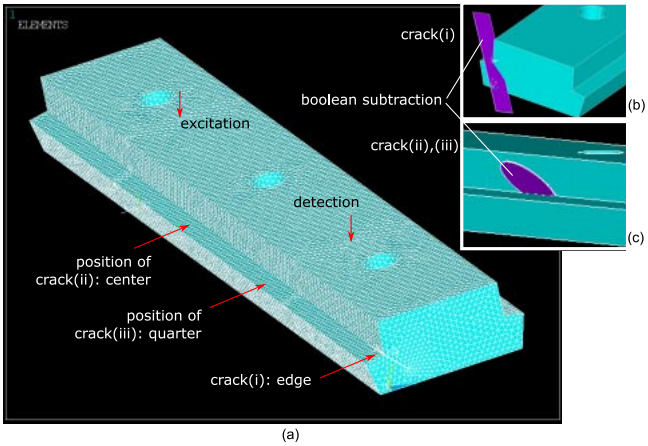

Fig. 12 (a) Finite element model of wedge specimen with crack (i). (b) Boolean operation of creating crack (i). (c) Bolean operation of creating crack (ii) and (iii).

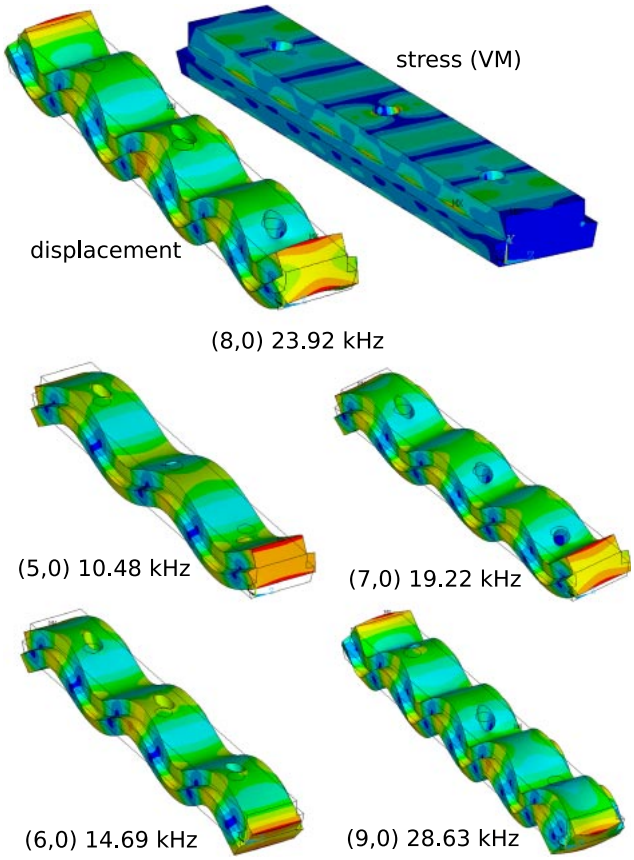

Fig. 13 (*m*,0) bending modes for frequency range of 10–40 kHz.

tetrahedral quadratic element with a size of 2 mm. The crack is created by performing a boolean difference operation on the original CAD model of the wedge as in Figs. 12(b) and 12(c). Models with cracks (ii) and (iii) are also created and analyzed independently. The input in the harmonic vibration analysis is a point excitation by an external force. The receiver acquires the displacement of the surface nodes at the measurement location. In the FEA, the evaluation is based on the gain of the transfer function of the displacement amplitude, $G_{\mathrm{u}} = |u_{(z)\mathrm{out}}/u_{(z)\mathrm{in}}|$. Three crack patterns are also considered in the analysis to evaluate the effect of the crack location. Crack (i) in Fig. 12 has the same location and shape as the experimental crack in Fig. 11. Cracks (ii) and (iii) are created using a cylindrical tool with a height of 0.3 mm and a radius of 10 mm at an elevation angle of 45° and a depth of 5 mm. Crack (ii) is located at the center of the bar, while crack (iii) is located at a quarter length from the bar end.

The modes of the original wedge in the 10–40 kHz frequency range are analyzed. The modes can be roughly classified into four types on the basis of the number of nodes.

Figure 13 shows (5–9,0) bending modes, where bending occurs only in the length direction. The number of nodes in the (length, width) direction distinguishes the bending vibration modes. As a representative example, the stress distribution of the (8,0) mode is displayed. Although this mode group exists from a relatively low frequency, the stress is almost zero around the crack(i)-prone area, and hardly any modal frequency shift of these modes is expected.

Figure 14 shows (1–4,2) modes, which are bending modes with two nodes in the width direction. The (2,2) mode does not appear in the frequency response because of the driving position. A significant resonant frequency shift can be expected since these modes have high stress near the crack(i)-prone area.

Figure 15 shows the (V2–6) longitudinal vibration modes. In the longitudinal vibration mode, almost no stress is generated at the edge of the member; thus, hardly any frequency shift because of the preferred site (i) is expected.

Figure 16 shows the (H4–6) modes originating from the opening and closing of through holes. The obtained vibration patterns are similar to that of the (*m*,2) mode, and the peak shift is expected in the (H4) mode because high stress is generated around crack(i)-prone area. However,

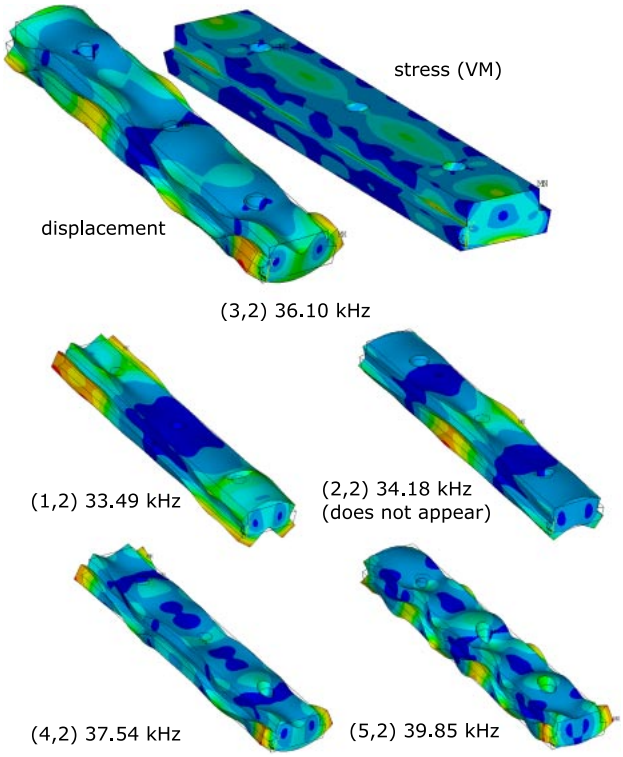

Fig. 14 (m,2) bending modes for frequency range of 10–40 kHz.

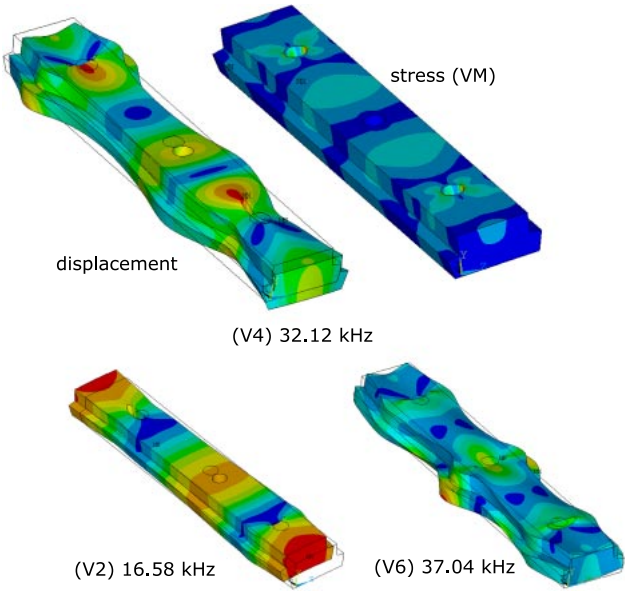

Fig. 15 Longitudinal modes for frequency range of 10–40 kHz.

hardly any shift is expected in the (H5) and (H6) modes since almost zero stress is generated at the edge.

3.2. Frequency Response Results

Figure 17 shows the acquired frequency characteristics in every 5 Hz. The experimental values in (a) and (c) are

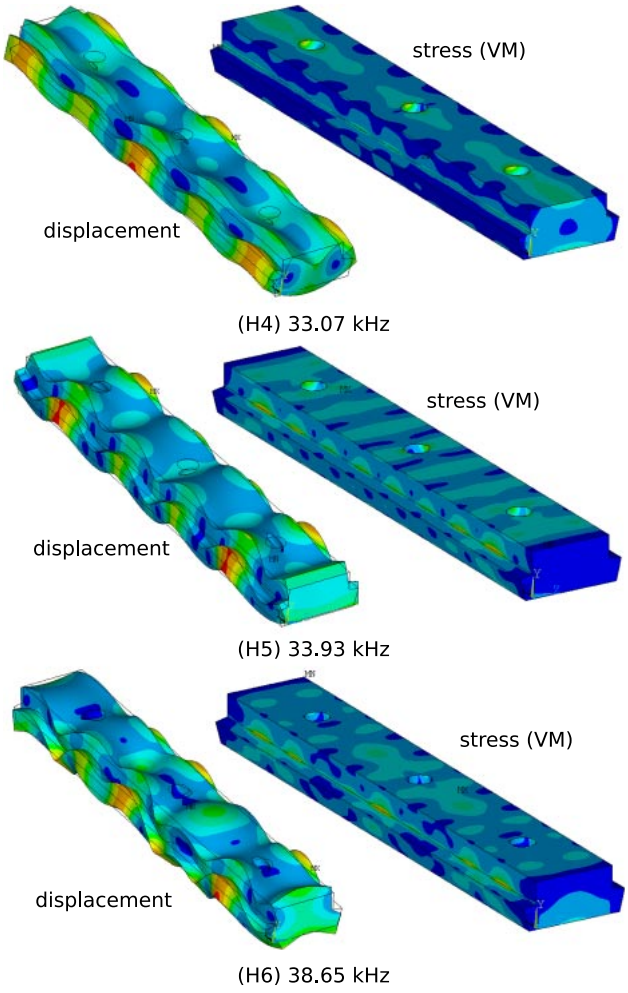

Fig. 16 Hole-related modes for frequency range of 10–40 kHz.

the voltage gain G_V measured with the network analyzer, and those in (b) and (d) are the displacement gain G_u calculated through the FEA. Although there is a slight difference in the position of the peak, some of the modes in the 30–40 kHz range are shifted to the lower-frequency side by the crack in both the experiment and the FEA. Figure 18 shows the frequency shift of these modes. The bending modes (m,0) with no nodal line in the width direction and the longitudinal vibration mode (V) show almost no shift in the case of crack (i), both of which are subjected to almost zero stress at the end of the member. In contrast, the bending vibration modes (m,2) with two nodal lines in the width direction exhibit shifts of 10 Hz order, and the shift direction is consistent between the experiment and the analysis. This is because the modes with bending in the width direction are subjected to higher stress at the crack site than in the surrounding area.

Despite the same crack size, the shift in the FEA is only about half of the experimental one. In addition, in the (m,0) and (H5,6) modes, a positive peak shift due to the decrease in edge mass is generated in the experimental data, which

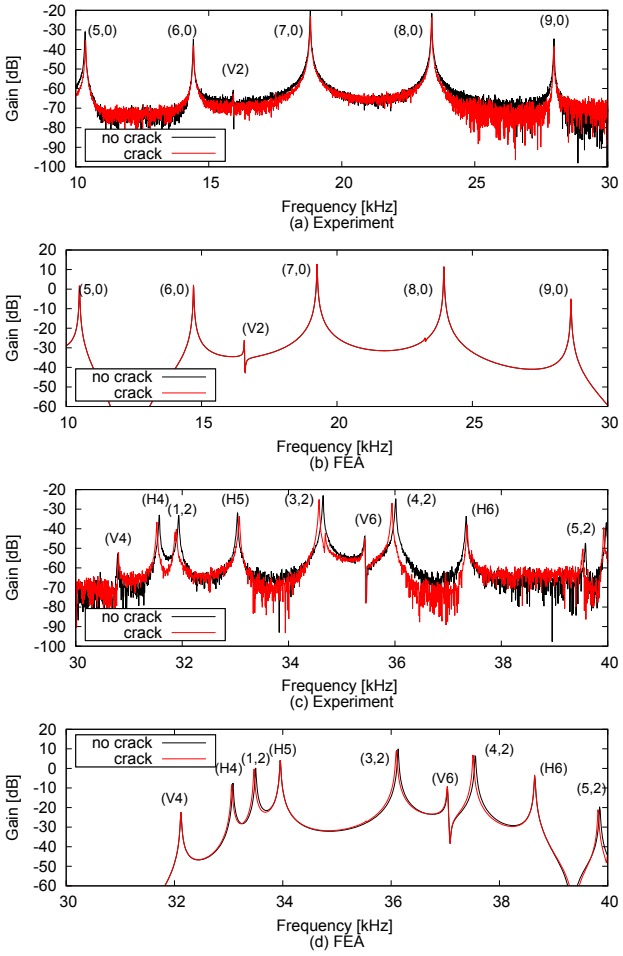

Fig. 17 Frequency characteristics with and without crack from (a), (c) experiment and (b), (d) finite element analysis. Note the almost complete overlap of the crack and no-crack lines in (b).

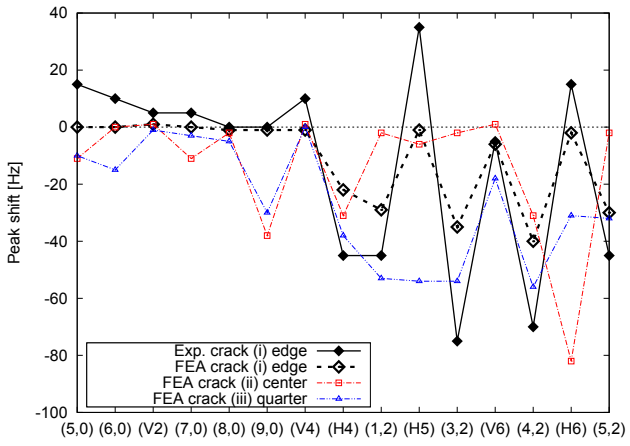

Fig. 18 Peak shift due to crack from experimental and finite element analysis results.

is not observed in the FEA. The cause of the error could be the difference in the void volume of the crack between the experiment and the FEA. In addition, tetrahedral elements larger than the crack width tend to have higher stiffness than in reality, which is unavoidable owing to the limitation in computational power.

When the crack position is varied, a peak shift is observed in the modes that did not respond to the edge crack (i). For example, the (H6) mode is highly responsive to the center crack (ii) and the (H5) mode is highly responsive to the quarter crack (iii). In addition, in the case of cracks (ii) and (iii), lower-order bending modes (m,0) respond. This is considered to result in the decrease in stiffness due to the crack at the high-stress site of each mode.

On the basis of this fact, we may locate a crack using the trend of the peak shift of each mode. At the same time, however, some modes are unaffected by the crack location. This means that it is necessary to detect the peak shift of a considerable number of modes such as (m,2) and (Hm) to judge the integrity of a member comprehensively, instead of focusing on one specific mode.

4. CONCLUSION

To evaluate the integrity of the rotor wedges of turbine generators, we proposed a diagnosis method based on the frequency response taken using a point-contact piezoelectric sensor. The natural frequencies of the wedge member were shifted to the lower side by a crack. First, we studied the dependence of the frequency shift on the crack shape in a two-dimensional T-shaped member. Then, we investigated the frequency shift of an actual wedge member. The specific modes were downshifted by a crack in both experiments and FEA. The possibility of utilizing the frequency shift for the detection of cracks was discussed.

In future work, it will be necessary to develop a practical setup to cope with an actual site where the wedge member is tightly held in the generator rotor slot. A method of compensating for the frequency shift due to contact with the iron core and for the environmental temperature drift should be developed. Since the contact load changes in a long-term generator operation, a method of removing this effect from the frequency response is necessary.

ACKNOWLEDGEMENT

The authors wish to acknowledge Mr. Hiroki Mine, Master's course student of Tokyo Tech. until March, 2021, for his help in the data acquisition for this study.

REFERENCES

[1] M. Šašić, B. Lloyd and A. Elez, "Finite element analysis of turbine generator rotor winding shorted turns," *IEEE Trans. Energy Convers.*, **27**, 930–937 (2012).

[2] X. Guorui, L. Xiaofang, K. Jinping, L. Yingli and L. Wei, "The influence of turbine generator rotor damping structure and material on first swing stability," *Electr. Power Syst. Res.*, **124**, 181–189 (2015).

[3] Y. Xiao, L. Zhou, J. Wang and J. Liu, "Design and performance analysis of magnetic slot wedge application in double-fed asynchronous motor-generator by finite-element method," *IET Electr. Power Appl.*, **12**, 1040–1047 (2018).
[4] H. Katayama, F. Sato, Y. Gunji, T. Ishikawa, A. Matsuzaki and H. Shimada, "Toshiba robotic inspection technology for turbo-generator," *Water Energy Int.*, **62r**, 19–23 (2019).
[5] DEKRA, "Ultrasonic testing for in situ generator inspection," https://www.dekra.com/en/ultrasonic-testing-for-in-situ-generator-inspection/ (Accessed 19 Aug. 2021).
[6] E. P. Papadakis, Ed., *Ultrasonic Instruments and Devices* (Academic Press, San Diego, 2000).
[7] D. U. Noiseux, "Measurement of power flow in uniform beams and plates," *J. Acoust. Soc. Am.*, **47**, 238–247 (1970).
[8] P. Cornwell, S. Doebling and C. Farrar, "Application of the strain energy damage detection method to plate-like structures," *J. Sound Vib.*, **224**, 359–374 (1999).
[9] D. Hutchins, D. Jansen and C. Edwards, "Lamb-wave tomography using non-contact transduction," *Ultrasonics*, **31**, 97–103 (1993).
[10] T. Ghosh, T. Kundu and P. Karpur, "Efficient use of lamb modes for detecting defects in large plates," *Ultrasonics*, **36**, 791–801 (1998).
[11] E. V. Malyarenko and M. K. Hinders, "Ultrasonic lamb wave diffraction tomography," *Ultrasonics*, **39**, 269–281 (2001).
[12] T. Kundu, *Ultrasonic Nondestructive Evaluation: Engineering and Biological Material Characterization* (CRC Press, Boca Raton, 2003).
[13] H. Nishino, T. Tanaka, K. Yoshida and J. Takatsubo, "Simultaneous measurement of the phase and group velocities of lamb waves in a laser-generation based imaging method," *Ultrasonics*, **52**, 530–535 (2012).
[14] W. D. Wallace, J. R. Houck, R. Bowers, B. W. Maxfield and M. R. Gaerttner, "Transducerless method for ultrasonic flaw testing in metals," *Rev. Sci. Instrum.*, **39**, 1863–1864 (1968).
[15] R. Thompson, G. Alers and M. Tennison, "Application of direct electromagnetic lamb wave generation to gas pipeline inspection," *Proc. IEEE IUS*, pp. 91–94 (1972).
[16] A. Osumi, T. Saito and Y. Ito, "Improved method of imaging defect in noncontact and nondestructive technique by high-intensity aerial burst ultrasonic wave and optical equipment," *Jpn. J. Appl. Phys.*, **54**, 07HC07 (2015).
[17] A. Osumi, K. Yamada, Y. Asada and Y. Ito, "Harmonic imaging of a defect in a flat plate using a guided wave generated by a high-intensity aerial ultrasonic wave," *Jpn. J. Appl. Phys.*, **58**, SGGB14 (2019).
[18] K. Yamanaka, T. Mihara and T. Tsuji, "Evaluation of closed cracks by model analysis of subharmonic ultrasound," *Jpn. J. Appl. Phys.*, **43**, 3082–3087 (2004).
[19] Y. Ohara, J. Potter, H. Nakajima, T. Tsuji and T. Mihara, "Multi-mode nonlinear ultrasonic phased array for imaging closed cracks," *Jpn. J. Appl. Phys.*, **58**, SGGB06 (2019).
[20] Y. Ohara, T. Umezaki, E. Carcreff, S. Haupert, T. Tsuji and T. Mihara, "Experimental analysis of linear and nonlinear ultrasonic scatterings at closed fatigue crack using fixed-voltage fundamental wave amplitude difference with radarlike display," *Jpn. J. Appl. Phys.*, **60**, SDDB01 (2021).
[21] T. Matsui, K. Tatsumi, T. Kawashima, Y. Murakami, N. Hozumi and T. Matsumoto, "Frequency determination in nondestructive test of semiconductor devices with ultrasound heating," *Jpn. J. Appl. Phys.*, **59**, SKKB07 (2020).
[22] K. Shimizu, A. Osumi and Y. Ito, "High-speed imaging of defects in thin plate by scanning elastic wave source technique using an airborne ultrasound phased array," *Jpn. J. Appl. Phys.*, **59**, SKKD15 (2020).
[23] I. Solodov, J. Bai, S. Bekgulyan and G. Busse, "A local defect resonance to enhance acoustic wave-defect interaction in ultrasonic nondestructive evaluation," *Appl. Phys. Lett.*, **99**, 211911 (2011).
[24] T. Arai, T. Yagi and H. Torii, "Defect detection device and defect detection method," Japan Patent JP2008-232763A (2006).
[25] D. Koyama, K. Nakamura, S. Ueha, H. Takahashi, K. Nukui and K. Ikeda, "A method for measuring liquid level using the flexural vibrations in a rod," *Acoust. Sci. & Tech.*, **29**, 274–282 (2008).
[26] K. Hasebe, Y. Mizuno and K. Nakamura, "Non-contact alignment-free soundness evaluation of adhesive anchors by exciting/detecting longitudinal bolt vibrations using electromagnetic acoustic waves," *Acoust. Sci. & Tech.*, **38**, 225–228 (2017).
[27] S. Takata, H. Inoue and S. Shinoda, "Proposal of the pipe diagnosis method using in-plane bending vibration of cylindrical shell," *Trans. JSME*, **84**, 17-00522–17-00522 (2018).
[28] P. Moczo, J. Kristek and E. Bystrický, "Efficiency and optimization of the 3-d finite-difference modeling of seismic ground motion," *J. Comput. Acoust.*, **9**, 593–609 (2001).
[29] B. Sarens, B. Verstraeten, C. Glorieux, G. Kalogiannakis and D. Van Hemelrijck, "Investigation of contact acoustic nonlinearity in delaminations by shearographic imaging, laser doppler vibrometric scanning and finite difference modeling," *IEEE Trans. Ultrason. Ferroelectr. Freq. Control*, **57**, 1383–1395 (2010).
[30] W. Lord, R. Ludwig and Z. You, "Developments in ultrasonic modeling with finite element analysis," *J. Nondestruct. Eval.*, **9**, 129–143 (1990).
[31] W. Ke, M. Castaings and C. Bacon, "3d finite element simulations of an air-coupled ultrasonic ndt system," *NDT & E Int.*, **42**, 524–533 (2009).
[32] C. Zhang and J. Achenbach, "Numerical analysis of surface-wave scattering by the boundary element method," *Wave Motion*, **10**, 365–374 (1988).
[33] D. Placko and T. Kundu, *DPSM for Modeling Engineering Problems* (Wiley-Interscience, Hoboken, 2007).
[34] O. C. Zienkiewicz, *The Finite Element Method*, 3rd expanded and rev. ed. (McGraw-Hill, London, 1977).
[35] National Astronomical Observatory of Japan, Ed., *Chronological Scientific Tables 2014* (Maruzen, Tokyo, 2013), pp. 394–395.
[36] C. L. Chow and R. C. Owen, "Fracture toughness measurement of mild steels with reinforced-double-cantilever-beam specimen," *J. Strain Anal. Eng.*, **11**, 195–201 (1976).
[37] J. Lancaster, *Engineering Catastrophes*, 3rd ed. (Woodhead Publishing, Cambridge, 2005), Chap. 4, pp. 139–189.
[38] A. S. Tetelman and A. J. McEvily, *Fracture of Structural Materials* (Wiley, New York, 1967), Chap. 2, pp. 48–49.
[39] T. Matsushita and S. Kimata, "Rotor of rotating machine," Japan Patent JP2006-296064A (2006).